Experimental realization of two-dimensional synthetic spin–orbit coupling in ultracold Fermi gases

Lianghui Huang[1,2], Zengming Meng[1,2], Pengjun Wang[1,2], Peng Peng[1,2], Shao-Liang Zhang[3], Liangchao Chen[1], Donghao Li[1], Qi Zhou[3]★ and Jing Zhang[1,4]★

Spin–orbit coupling (SOC) is central to many physical phenomena, including fine structures of atomic spectra and topological phases in ultracold atoms. Whereas, in general, SOC is fixed in a system, laser–atom interaction provides a means to create and control synthetic SOC in ultracold atoms[1]. Despite significant experimental progress in this area[2–8], two-dimensional (2D) synthetic SOC, which is crucial for exploring two- and three-dimensional topological phases, is lacking. Here, we report the experimental realization of 2D SOC in ultracold 40K Fermi gases using three lasers, each of which dresses one atomic hyperfine spin state. Through spin-injection radiofrequency (rf) spectroscopy[4], we probe the spin-resolved energy dispersions of the dressed atoms, and observe a highly controllable Dirac point created by the 2D SOC. These results constitute a step towards the realization of new topological states of matter.

There have been many theoretical proposals for creating multi-dimensional SOC in ultracold atoms[9–14], so as to access novel macroscopic quantum phenomena and quantum topological states[15–24]. Whereas these proposals have not been realized in laboratories, physicists have also just begun to explore topological phenomena in optical lattices[25–28]. Here, we use the Raman scheme to produce a highly controllable 2D synthetic SOC for an ultracold Fermi gas of 40K. Such SOC allows us to create and manipulate a single stable Dirac point on a 2D plane, which is detected by spin-injection rf spectroscopy[4].

We apply three far-detuned lasers propagating on the x–y plane to couple three ground hyperfine spin states, within the $4^2S_{1/2}$ ground electronic manifold, $|1\rangle = |F = 9/2, m_F = 3/2\rangle$, $|2\rangle = |F = 9/2, m_F = 1/2\rangle$ and $|3\rangle = |F = 7/2, m_F = 1/2\rangle$, where (F, m_F) are the quantum numbers for hyperfine spin states as shown in Fig. 1a, to the electronically excited states. Unlike the tripod scheme, where a single excited state is considered[9–11,15–18], in the 40K used here the excited states include a fine-structure doublet $4^2P_{1/2}$ (D$_1$ line) and $4^2P_{3/2}$ (D$_2$ line) with a fine-structure splitting of ~3.4 nm. Each of two D-line components also has hyperfine structures. After adiabatically eliminating excited states, the ring scheme proposed in ref. 12 is realized for three cyclically coupled states, with a generalization to arbitrary laser configurations.

The Hamiltonian is written as

$$H = \sum_{i=1}^{3} \left(\frac{\mathbf{p}^2}{2m} + \varepsilon_i \right) |i\rangle\langle i| + \sum_{j=1}^{n} E_j |j\rangle\langle j|$$
$$+ \sum_{i=1}^{3} \left(\Omega_i e^{i(\mathbf{k}'_i \cdot \mathbf{r} + \omega_i t + \theta_i)} \left(\sum_{j=1}^{n} M_{ji} |j\rangle\langle i| \right) + \text{h.c.} \right) \quad (1)$$

where $\mathbf{p}$ denotes the momentum of atoms, $\mathbf{k}'_i$ ($|\mathbf{k}'_i| = 2\pi/\lambda_i$) and ω_i are the wavevectors and frequencies of the three lasers, Ω_i are the Rabi frequencies, i, j are the indices for the three ground hyperfine spin and the excited states respectively, ε_i and E_j are the ground and excited state energies, n is the total number of the excited states and M_{ij} is the matrix element of the dipole transition. Different from refs 9,10,15, each hyperfine ground spin state here is dressed by only one laser field, regardless of the excited states it is coupled to. A gauge transformation, $|i\rangle \rightarrow e^{-i(\mathbf{k}'_i \cdot \mathbf{r} + \theta_i)}|i\rangle$, is applied to eliminate the phase θ_i. All results discussed here are therefore insensitive to the phase difference, and the sophisticated and challenging phase lockings are no longer necessary.

Applying the rotating wave approximation and the adiabatic elimination of excited states, the Hamiltonian is written as $H_a = p_z^2/(2m) + H_{xy}$,

$$H_{xy} = \sum_{i=1}^{3} \left(\frac{(\mathbf{p} - \mathbf{k}_i)^2}{2m} + \delta_i \right) |i\rangle\langle i| - \sum_{i' \neq i} \frac{\Omega_{ii'}}{2} |i\rangle\langle i'| \quad (2)$$

The light-induced energy shifts in the adiabatic elimination have been recast into the diagonal terms, δ_1 is set as zero (energy reference) for simplification, δ_2 (δ_3) corresponds to the two-photon Raman detuning between Raman laser 1 and 2 (1 and 3), and $\mathbf{k}_i = \hbar\mathbf{k}'_i$. All three $\Omega_{ii'} = \Omega_{i'i}$ are real Raman coupling strengths regarding $|i\rangle \leftrightarrow |i'\rangle$. Their values are derived from calculations (see Supplementary Information) and measured in experiments[3]. The single-photon recoil momentum $k_r = 2\pi\hbar/\lambda$ and recoil energy $E_r = k_r^2/2m$ are taken as natural momentum and energy units. Since the dispersion along the z direction is not affected by the lasers, we will focus on the 2D Hamiltonian H_{xy}.

[1]State Key Laboratory of Quantum Optics and Quantum Optics Devices, Institute of Opto-Electronics, Shanxi University, Taiyuan 030006, China. [2]Collaborative Innovation Center of Extreme Optics, Shanxi University, Taiyuan 030006, China. [3]Department of Physics, The Chinese University of Hong Kong, Shatin, New Territories, Hong Kong. [4]Synergetic Innovation Center of Quantum Information and Quantum Physics, University of Science and Technology of China, Hefei, Anhui 230026, China. *e-mail: qizhou@phy.cuhk.edu.hk; jzhang74@sxu.edu.cn, jzhang74@yahoo.com
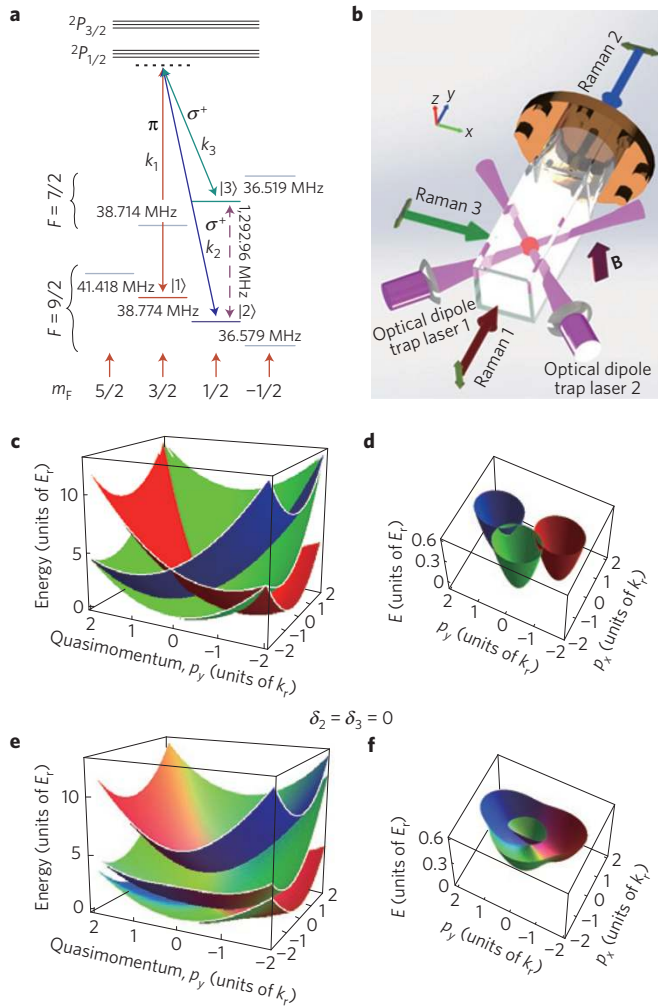
Figure 1 | Two-dimensional synthetic spin–orbit coupling. a, Schematic of energy levels of ^{40}K for creating 2D SOC. Each of the three Raman lasers dresses one hyperfine spin state from $|9/2, 3/2\rangle$ ($|1\rangle$), $|9/2, 1/2\rangle$ ($|2\rangle$) and $|7/2, 1/2\rangle$ ($|3\rangle$). Atoms are initially prepared in the free reservoir spin state $|9/2, 5/2\rangle$. **b**, Experimental geometry and laser configuration. Raman lasers 1 and 2 counter-propagate along the y axis and Raman laser 3 propagates along the x axis, and they are linearly polarized along the z, x and y directions respectively. **c**, Energy–momentum dispersions in the absence of SOC ($\Omega_{12} = \Omega_{13} = \Omega_{23} = 0$). The three parabolae are displaced from the origin by $\mathbf{k}_i$, respectively, in the (p_x, p_y) plane. **e**, Energy–momentum dispersions of three dressed states after turning on SOC ($-\Omega_{12} = 2\Omega_{13} = 2\Omega_{23} = E_r$), showing that the dispersions of two dressed states touch at a Dirac point. Here, $\delta_2 = \delta_3 = 0$. **d,f**, Plots enlarging the low-energy parts of **c** and **e**, respectively. In **e,f**, the weights of different hyperfine spin states in the dressed states—the eigenstates of the Hamiltonian with SOC—are represented by assigning different colours to the hyperfine spin states. Red, blue and green represent $|1\rangle$, $|2\rangle$ and $|3\rangle$ respectively. The depth of each colour indicates the percentage of the corresponding spin state in a dressed state.

Using the two lemmas in Supplementary Information, we find that a doubly degenerate point $\mathbf{p}_0$ exists in the momentum space, where $\mathbf{p}_0$ satisfies two independent equations

$$-\frac{(\mathbf{k}_1 - \mathbf{k}_2) \cdot \mathbf{p}_0}{m} + \delta_1 - \delta_2 = -\frac{\Omega_{12}\Omega_{13}}{2\Omega_{23}} + \frac{\Omega_{12}\Omega_{23}}{2\Omega_{13}}$$

$$-\frac{(\mathbf{k}_2 - \mathbf{k}_3) \cdot \mathbf{p}_0}{m} + \delta_2 - \delta_3 = -\frac{\Omega_{12}\Omega_{23}}{2\Omega_{13}} + \frac{\Omega_{13}\Omega_{23}}{2\Omega_{12}} \quad (3)$$

Projecting the Hamiltonian in equation (2) to the pseudo-spin-1/2 formed by the two dressed states near the degenerate point $\mathbf{p}_0$, an effective Hamiltonian at low energies is obtained,

$$H_{SO} = (\lambda_{x1}p_x + \lambda_{y1}p_y)\sigma_x + (\lambda_{x2}p_x + \lambda_{y2}p_y)\sigma_z \quad (4)$$

where $p_{i=x,y}$ has been redefined as $p_i - p_{0,i}$ for simplicity. By rotating the momentum and the spin (see Supplementary Methods), the Hamiltonian can be simplified as

$$H_{SO} = \lambda_x p'_x \sigma'_x + \lambda_y p'_y \sigma'_z \quad (5)$$

where both λ_x and λ_y are finite. Equation (5) describes a 2D SOC, which is equivalent to the Dresselhaus coupling if a simple transformation $\sigma'_x \rightarrow \sigma'_y, \sigma'_z \rightarrow \sigma'_x$ is applied. Such a 2D SOC directly tells one that the doubly degenerate point at $\mathbf{p}_0$ corresponds to a Dirac point with a linear dispersion at low energies. In particular, both the amplitude and anisotropy λ_x/λ_y can be largely tuned (see Supplementary Information). As a demonstration, Figs 1e (1f) and 1c (1d) show a comparison of the energy–momentum dispersion with and without SOC. The latter shows that energy dispersions of two dressed states touch at a Dirac point.

In this experiment, a homogeneous bias magnetic field $B_0 = 121.4$ G along the z axis (the gravity direction shown in Fig. 1b) produces a Zeeman shift to isolate these three hyperfine spin states from other ones in the Raman transitions, as shown in Fig. 1a. When the three Raman lasers are nearly resonant with the three ground states ($\delta_{i=1,2,3} \approx 0$), the nearest Raman transitions with other hyperfine states are $|7/2, 3/2\rangle \leftrightarrow |2\rangle$ and $|7/2, 3/2\rangle \leftrightarrow |3\rangle$, which have large two-photon Raman detunings about $h \times 60$ kHz. A three-level system is thus a good description of our experiment.

The Raman coupling strength $\Omega_{ii'}$ includes contributions from all excited states of two D-line components, as shown in Fig. 2a (see Supplementary Information). When the wavelength of the Raman lasers is longer than the D_1 line (770.1 nm) or shorter than the D_2 line (766.7 nm), $\Omega_{12}\Omega_{13}\Omega_{23} > 0$ (see the eigenvalues of dressed states in Supplementary Information), the Dirac point emerges in the highest two dressed states, as shown in Fig. 2b,d. In contrast, when the wavelength of the Raman lasers is tuned between the D_1 line and D_2 line, $\Omega_{12}\Omega_{13}\Omega_{23} < 0$, the Dirac point emerges when the lowest two dressed states become degenerate, as shown in Fig. 2c. This is different from the work in ref. 19, where only one excited state is considered and far-blue-detuned lasers are used to make the degenerate dark states the low-lying ones in the manifold of ground electronic states.

We investigate the energy–momentum dispersions of three dressed states by spin-injection rf spectroscopy, which drives the atoms from a free spin-polarized state into SOC dressed states. We start with a degenerate Fermi gas of 2×10^6 ^{40}K atoms at the free reservoir spin state $|9/2, 5/2\rangle$ in a crossed optical dipole trap. A homogeneous bias magnetic field is ramped to $B_0 = 121.4$ G. Then the three Raman lasers are ramped up in 60 ms from zero to their final value. Subsequently, a Gaussian shape pulse of the rf field is applied for 450 μs to drive atoms from $|9/2, 5/2\rangle$ to the final empty state with 2D SOC. The rf field does not transfer momentum to the atoms, and spin injection occurs when its frequency matches the energy difference between the initial and final states. Since the spin state $|9/2, 5/2\rangle$ is coupled via rf to the state $|1\rangle$, rf spectroscopy also measures the weight of the $|1\rangle$ state, in addition to the energy dispersions with 2D SOC. Following the spin-injection process, the Raman lasers, the optical trap and the magnetic field are switched off abruptly, and atoms freely expand for 12 ms in a magnetic field gradient applied along the x axis. Absorption images are taken along the z direction. By counting the number of atoms in state $|1\rangle$ as a function of the momentum and the rf frequency from
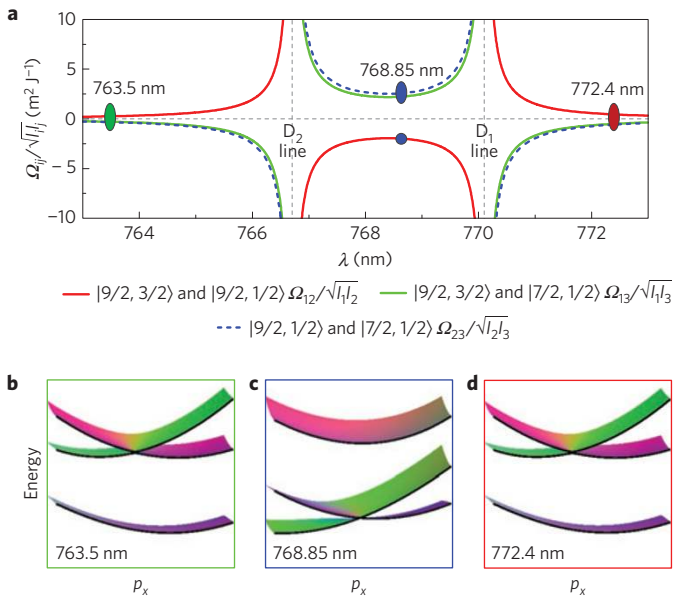
Figure 2 | Controlling the Dirac point by changing the wavelength of the Raman lasers. a, Red, green and blue curves represent the Raman coupling strength Ω_{12}, Ω_{13} and Ω_{23} as functions of the wavelength λ of the Raman lasers. Depending on λ, $\Omega_{12}\Omega_{13}\Omega_{23}$ can be either positive or negative. I_i is the intensity of the ith laser. **b–d**, Energy bands for wavelengths of 763.5 nm (blue-detuning D_2 line), 768.85 nm (between D_1 and D_2 line) and 772.4 nm (red-detuning D_1 line), respectively. The two higher dispersions touch at the Dirac point in **b** and **d**, where $\Omega_{12}\Omega_{13}\Omega_{23}$ is positive. The two lower dispersions touch at the Dirac point in **c**, where $\Omega_{12}\Omega_{13}\Omega_{23}$ is negative.

the absorption image, we determine the energy band structure and locate the Dirac point.

Figure 3a2 shows the momentum-resolved spin-injection spectrum when the one-photon detuning of the Raman lasers is set at a wavelength of 772.4 nm (red-detuning D_1); the corresponding theoretical plot is shown in Fig. 3a1. The two higher-energy dispersions touch at a Dirac point, as shown in Fig. 3a2. To further visualize the Dirac point, we plot the energy as a function of p_y for various p_x, as shown in Fig. 3a3–a5. When the wavelength of the Raman lasers is tuned to 768.85 nm, between the D_1 line and D_2 line, two lower-energy dispersions touch at a Dirac point, as shown in Fig. 3b1–b5. These two wavelengths were used to investigate the 1D SOC (refs 3,5). For the wavelength of the Raman lasers at the 763.5 nm blue-detuning D_2 line, we have observed that two higher-energy dispersions touch at a Dirac point, similar to the 772.4 nm case. We also perform numerical calculations for the eigenvalues of the Hamiltonian in equations (2) and (5) according to experimental parameters and have found a reasonably good agreement between theory and experiments. In practice, several mechanisms, such as the fluctuation of the magnetic field and the finite momentum resolution, lead to the differences in rf spectrum between the theoretical and experimental results, as well as the error bars presented in Fig. 3 (see Supplementary Information).

Although a pair of Dirac points has been produced in optical lattices[25], to our best knowledge, we have created a single Dirac point for the first time in the continuum. Moreover, the Dirac point created in this scheme is robust, in the sense that it moves in momentum space without opening a gap when experimental parameters change. This is because the Hamiltonian in equation (2) is real—consequently, the SOC in equation (5) cannot contain the σ_y term. By modulating δ_i, Ω_i and $\mathbf{k}_i$, an arbitrary trajectory of the Dirac point in the momentum space can in principle be designed. As a demonstration, we fix δ_2 and measure the positions of the Dirac point on the (p_x, p_y) plane as a function of δ_3, as shown
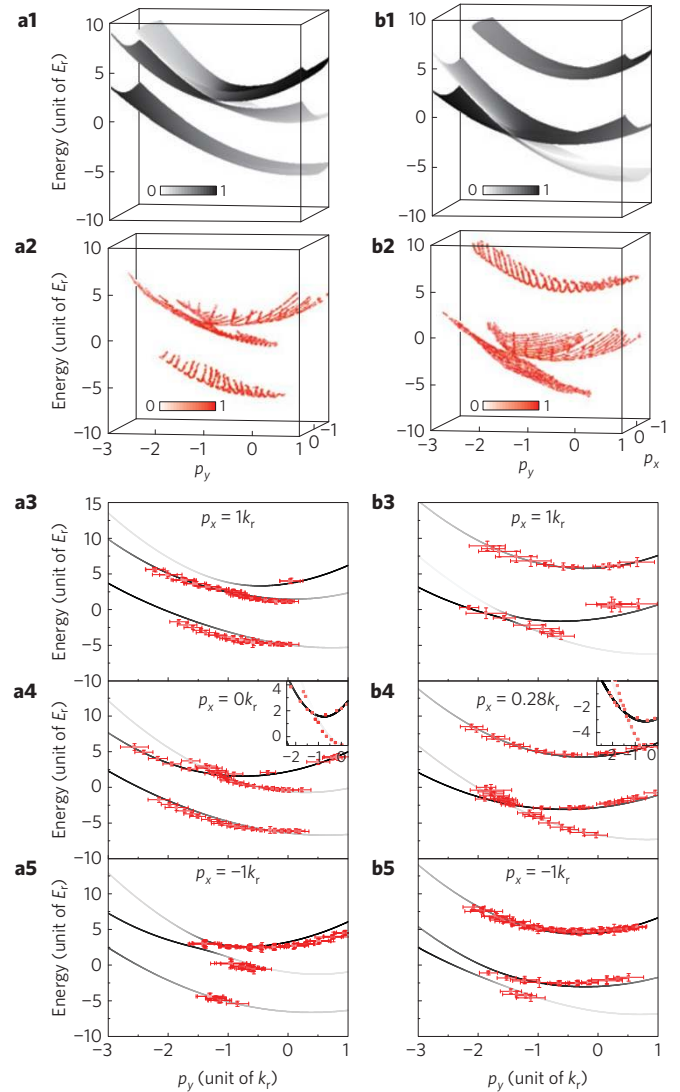
Figure 3 | Energy dispersions of dressed atoms measured by rf spin-injection spectroscopy. a1–a5, The one-photon detuning of the Raman lasers is set at a wavelength of 772.4 nm (red-detuning D_1). $\Omega_{12}=3.58E_r$, $\Omega_{13}=-3.94E_r$, $\Omega_{23}=-4.66E_r$, $\delta_2=-5.14E_r$, $\delta_3=-3.23E_r$. **b1–b5**, The wavelength is set at 768.85 nm, between the D_1 line and D_2 line. $\Omega_{12}=-4.96E_r$, $\Omega_{13}=5.46E_r$, $\Omega_{23}=6.46E_r$, $\delta_2=-5.2E_r$, $\delta_3=-2.13E_r$. **a1,b1**, Theoretical results for the $|1\rangle$ component using the realistic experimental parameters. **a2,b2**, Experimental results measured by rf spin-injection spectroscopy. Each line on the surfaces of the dispersions is constructed from time-of-flight images at the given rf frequency (see Supplementary Information). **a3–a5**, Cross-section drawings of **a1** and **a2** in energy-p_y coordinates for different quasimomenta p_x. Red dots with error bars and solid curves are experimental and theoretical results, respectively. The inset in **a4** is a plot (without error bars) enlarging the region near the Dirac point. Here, $\lambda_{x1}=0$, $\lambda_{x2}=-0.42k_r/m$, $\lambda_{y1}=1.5k_r/m$, and $\lambda_{y2}=-0.07k_r/m$ are obtained by the experimental parameters. **b3–b5**, Cross-section drawings of **b1** and **b2**. The inset in **b4** is a plot enlarging the region near the Dirac point. λ_{x1}, $\lambda_{x2}\lambda_{y1}$ and λ_{y2} are the same as in **a**, since Ω_{12}/Ω_{13} and Ω_{12}/Ω_{23} remain the same.

in Fig. 4a (blue dots). When fixing δ_3 and changing δ_2, the Dirac point moves along a different line (red dots). We also measure the energy at the Dirac point, as well as the energy separation ΔE from highest dressed state, as a function of the Raman coupling strength. Zero energy in Fig. 4b corresponds to the Zeeman energy splitting between $|9/2, 5/2\rangle$ and $|9/2, 3/2\rangle$. The energy of the Dirac point
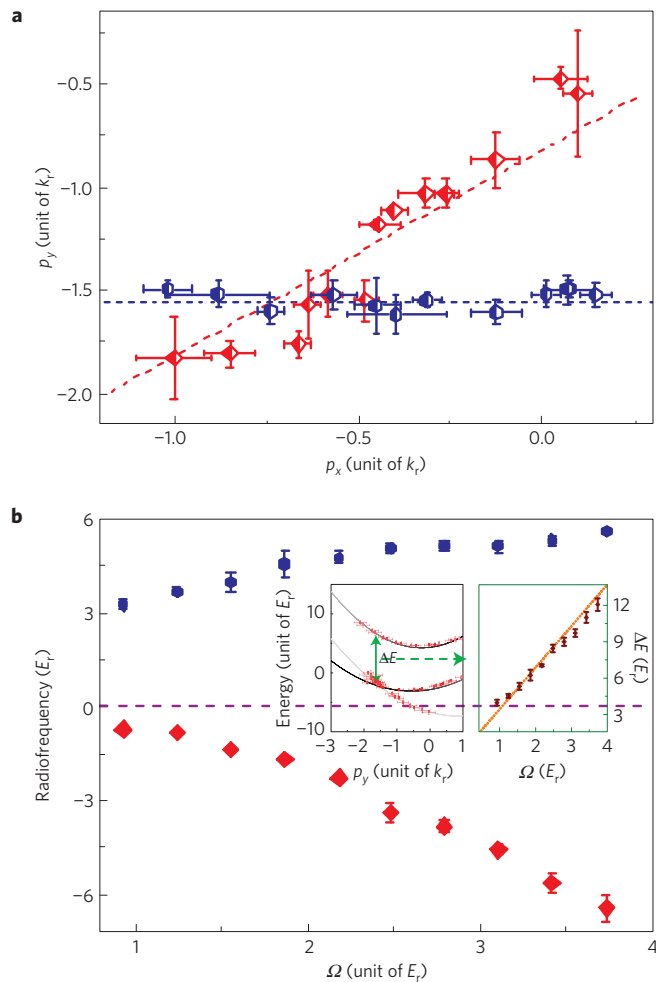
Figure 4 | Moving the Dirac point. a, Controlling the Raman detuning δ_2 and δ_3, the Dirac point moves along certain trajectories in momentum space. Blue dots: δ_2 is fixed at $-5.45E_r$ and δ_3 is tuned in the range $[-2E_r, 0.45E_r]$. Red dots: δ_3 is fixed at $-0.2E_r$ and δ_2 is tuned in the range $[-7E_r, -2.5E_r]$. The other parameters are $\Omega_{12} = -4.96E_r$, $\Omega_{13} = 5.46E_r$, $\Omega_{23} = 6.46E_r$. **b**, Energy at the Dirac point (red diamonds) and corresponding energy of the highest dressed state with the same momentum $\mathbf{p}_0$ (blue boxes) as a function of the Raman coupling strength. $-\Omega_{12} = 0.91\Omega_{13} = 0.77\Omega_{23} = \Omega$, $\delta_2 = -5.2E_r$ and $\delta_3 = -2.13E_r$. The left inset in **b** shows the energy dispersions. The right inset in **b** represents the energy separation ΔE between the Dirac point and the highest dressed state as a function of the Raman coupling strength. Here, the one-photon detuning of three Raman lasers is at a wavelength of 768.85 nm. The error bars represent the standard deviation of repeated measurements.

decreases with increasing Raman coupling strength (red diamonds). ΔE increases linearly with increasing Raman coupling strength (right inset of Fig. 4b). Since the diagonal energy shift induced by the Raman field has no influence on the effective SOC, we further plot the energy difference between the Dirac point and the highest dressed state, as highlighted by the green vertical arrow in the left inset of Fig. 4b. We find that ΔE increases linearly with increasing Raman coupling strength (right inset of Fig. 4b), and observe a good agreement between experimental and theoretical results.

We hope that a highly controllable 2D SOC will help physicists to explore both gapless topological matter in the continuum, analogous to graphene and Weyl semimetals in lattices, and interesting topological or other exotic superfluids when the gap at the Dirac point is opened[20–24]. Whereas our scheme is very general and can be applied to any atomic species, we hope that the specific heating

effect in alkali atoms due to the fine-structure splitting may be overcome by novel cooling schemes or the quantum quenching approach, which may allow one to extract topological properties from quantum dynamics in a relatively short timescale[29].

Methods

Methods and any associated references are available in the online version of the paper.

References

1. Dalibard, J., Gerbier, F., Juzeliūnas, G. & Öhberg, P. Artificial gauge potentials for neutral atoms. *Rev. Mod. Phys.* **83,** 1523–1543 (2011).
2. Lin, Y.-J., Jiménez-García, K. & Spielman, I. B. Spin–orbit-coupled Bose–Einstein condensates. *Nature* **471,** 83–86 (2011).
3. Wang, P. *et al*. Spin–orbit coupled degenerate Fermi gases. *Phys. Rev. Lett.* **109,** 095301 (2012).
4. Cheuk, L. W. *et al*. Spin-injection spectroscopy of a spin–orbit coupled Fermi gas. *Phys. Rev. Lett.* **109,** 095302 (2012).
5. Williams, R. A., Beeler, M. C., LeBlanc, L. J. & Spielman, I. B. Raman-induced interactions in a single-component Fermi gas near an s-wave Feshbach resonance. *Phys. Rev. Lett.* **111,** 095301 (2013).
6. Zhang, J.-Y. *et al*. Collective dipole oscillations of a spin–orbit coupled Bose–Einstein condensate. *Phys. Rev. Lett.* **109,** 115301 (2012).
7. Qu, C., Hamner, C., Gong, M., Zhang, C. & Engels, P. Observation of Zitterbewegung in a spin–orbit coupled Bose–Einstein condensate. *Phys. Rev. A* **88,** 021604(R) (2013).
8. Olson, A. J. *et al*. Tunable Laudau–Zener transitions in a spin–orbit-coupled Bose–Einstein condensate. *Phys. Rev. A* **90,** 013616 (2014).
9. Unanyan, R. G., Shore, B. W. & Bergmann, K. Laser-driven population transfer in four-level atoms: consequences of non-Abelian geometrical adiabatic phase factors. *Phys. Rev. A* **59,** 2910–2919 (1999).
10. Ruseckas, J., Juzeliūnas, G., Öhberg, P. & Fleischhauer, M. Non-Abelian gauge potentials for ultracold atoms with degenerate dark states. *Phys. Rev. Lett.* **95,** 010404 (2005).
11. Juzeliūnas, G., Ruseckas, J. & Dalibard, J. Generalized Rashba–Dresselhaus spin–orbit coupling for cold atoms. *Phys. Rev. A* **81,** 053403 (2010).
12. Campbell, D. L., Juzeliūnas, G. & Spielman, I. B. Realistic Rashba and Dresselhaus spin–orbit coupling for neutral atoms. *Phys. Rev. A* **84,** 025602 (2011).
13. Xu, Z. F., You, L. & Ueda, M. Atomic spin–orbit coupling synthesized with magnetic-field-gradient pulses. *Phys. Rev. A* **87,** 063634 (2013).
14. Anderson, B. M., Spielman, I. B. & Juzeliūnas, G. Magnetically generated spin–orbit coupling for ultracold atoms. *Phys. Rev. Lett.* **111,** 125301 (2013).
15. Stanescu, T. D., Zhang, C. & Galitski, V. Nonequilibrium spin dynamics in a trapped Fermi gas with effective spin–orbit interactions. *Phys. Rev. Lett.* **99,** 110403 (2007).
16. Juzeliūnas, G., Ruseckas, J., Jacob, A., Santos, L. & Öhberg, P. Double and negative reflection of cold atoms in non-Abelian gauge potentials. *Phys. Rev. Lett.* **100,** 200405 (2008).
17. Vaishnav, J. Y. & Clark, C. W. Observing Zitterbewegung with ultracold atoms. *Phys. Rev. Lett.* **100,** 153002 (2008).
18. Larson, J. & Sjöqvist, E. Jahn–Teller-induced Berry phase in spin–orbit-coupled Bose–Einstein condensates. *Phys. Rev. A* **79,** 043627 (2009).
19. Zhang, Y., Mao, L. & Zhang, C. Mean-field dynamics of spin–orbit coupled Bose–Einstein condensates. *Phys. Rev. Lett.* **108,** 035302 (2012).
20. Zhang, C. Spin–orbit coupling and perpendicular Zeeman field for fermionic cold atoms: observation of the intrinsic anomalous Hall effect. *Phys. Rev. A* **82,** 021607(R) (2010).
21. Zhu, S.-L., Shao, L.-B., Wang, Z. D. & Duan, L.-M. Probing non-Abelian statistics of Majorana fermions in ultracold atomic superfluid. *Phys. Rev. Lett.* **106,** 100404 (2011).
22. Vyasanakere, J. P. & Shenoy, V. B. Bound states of two spin-$\frac{1}{2}$ fermions in a synthetic non-Abelian gauge field. *Phys. Rev. B* **83,** 094515 (2011).
23. Hu, H., Jiang, L., Liu, X.-J. & Han, P. Probing anisotropic superfluidity in atomic Fermi gases with Rashba spin–orbit coupling. *Phys. Rev. Lett.* **107,** 195304 (2011).
24. Yu, Z.-Q. & Zhai, H. Spin–orbit coupled Fermi gases across a Feshbach resonance. *Phys. Rev. Lett.* **107,** 195305 (2011).
25. Tarruell, L., Greif, D., Uehlinger, T., Jotzu, G. & Esslinger, T. Creating, moving and merging Dirac points with a Fermi gas in a tunable honeycomb lattice. *Nature* **483,** 302–305 (2012).

26. Jotzu, G. *et al.* Experimental realization of the topological Haldane model with ultracold fermions. *Nature* **515**, 237–240 (2014).
27. Aidelsburger, M. *et al.* Realization of the Hofstadter Hamiltonian with ultracold atoms in optical lattices. *Phys. Rev. Lett.* **111**, 185301 (2013).
28. Miyake, H., Siviloglou, G. A., Kennedy, C. J., Burton, W. C. & Ketterle, W. Realizing the Harper Hamiltonian with laser-assisted tunneling in optical lattices. *Phys. Rev. Lett.* **111**, 185302 (2013).
29. Setiawan, F., Sengupta, K., Spielman, I. B. & Sau, J. D. Dynamical detection of topological phase transition in short-lived atomic systems. *Phys. Rev. Lett.* **115**, 190401 (2015).

Author contributions
L.H., Z.M., P.W., P.P., L.C., D.L. and J.Z. performed experiments. S.-L.Z., Q.Z. and J.Z. did the theory. S.-L.Z., Q.Z., L.H., P.W. and J.Z. contributed to the theoretical modelling and explanation of the experimental data. Q.Z. and J.Z. wrote the paper. All authors discussed the results and commented on the manuscript. J.Z. supervised the project.

Additional information
Supplementary information is available in the online version of the paper. Reprints and permissions information is available online at www.nature.com/reprints. Correspondence and requests for materials should be addressed to Q.Z. or J.Z.

Competing financial interests
The authors declare no competing financial interests.

Methods

Experimental set-up. After sympathetic cooling with bosonic ^{87}Rb in a quadrupole-Ioffe configuration magnetic trap, ^{40}K atoms in the $|9/2, 9/2\rangle$ state and ^{87}Rb atoms in the $|2, 2\rangle$ are transferred into an optical dipole trap formed by two orthogonal 1,064 nm laser beams. The Fermi gas is further evaporatively cooled to $T/T_F \approx 0.3$, giving about 2×10^6 ^{40}K atoms with ^{87}Rb atoms in the optical trap[30], where T_F is the Fermi temperature defined by $T_F = (6N)^{1/3}\hbar\bar{\omega}/k_B$ and the geometric mean of trapping frequencies $\bar{\omega} \simeq 2\pi \times 80$ Hz in our system, N is the number of fermions. After removal of the ^{87}Rb atoms, the fermionic atoms are transferred into the state $|9/2, 5/2\rangle$ via a rapid adiabatic passage induced by a rf field of 80 ms at 19.6 G. Here, the transition is addressed by a rf ramp that starts at 6.56 MHz to the end of 6.28 MHz. Then a homogeneous bias magnetic field along the z axis (gravity direction) is ramped to $B_0 = 121.4$ G by a pair of coils operating in the Helmholtz configuration.

Raman lasers. Three Raman lasers are derived from a CW Ti–sapphire single frequency laser. Two Raman beams 1 and 2 are frequency-shifted around $+201.144 \times 2$ MHz and $+220.531 \times 2$ MHz by two double-pass acousto-optic modulators (AOM), respectively. Raman laser 3 is sent through two AOMs in double-pass and frequency-shifted -212.975×4 MHz. Then the three Raman beams are coupled into three polarization-maintaining single-mode fibres, respectively, in order to improve stability of the beam pointing and achieve a better beam-profile quality. After the fibres, these three Raman beams have maximum powers of 80 mW for each beam and overlap in the atomic cloud with $1/e^2$ radii of 200 μm. Raman lasers 1 and 2 counter-propagate along the y axis and Raman laser 3 propagates along the x axis, and they are linearly polarized along the z, x and y directions, respectively, corresponding to π, σ and σ polarizations relative to the quantization axis z shown in Fig. 1b.

References

30. Xiong, D. *et al*. Quantum degenerate Fermi–Bose mixtures of ^{40}K and ^{87}Rb atoms in a quadrupole-Ioffe configuration trap. *Chin. Phys. Lett.* **25**, 843–846 (2008).